

Magnetic properties of an individual *Magnetospirillum gryphiswaldense* cell

Mathias M. Claus,^{1,2} Marcus Wyss,¹ Dirk Schüler,³ Martino Poggio,^{1,2} and Boris Gross²

¹Swiss Nanoscience Institute, University of Basel, Klingelbergstrasse 82, 4056 Basel, Switzerland

²Department of Physics, University of Basel, Klingelbergstrasse 82, 4056 Basel, Switzerland

³Lehrstuhl für Mikrobiologie, University of Bayreuth, Universitätsstraße 30, 95447 Bayreuth, Germany

(Dated: March 19, 2024)

Many bacteria share the fascinating ability to sense Earth’s magnetic field — a process known as magnetotaxis. These bacteria synthesize magnetic nanoparticles, called magnetosomes, within their own cell body and arrange them to form a linear magnetic chain. The chain, which behaves like a compass needle, aligns the microorganisms with the geomagnetic field. Here, we measure the magnetic hysteresis of an individual bacterium of the species *Magnetospirillum gryphiswaldense* via ultrasensitive torque magnetometry. These measurements, in combination with transmission electron microscopy and micromagnetic simulations, reveal the magnetic configurations of the magnetosomes, their progression as a function of applied field, as well as the total remanent magnetic moment and effective magnetic anisotropy of a chain within a single bacterium. Knowledge of magnetic properties is crucial both for understanding the mechanisms behind magnetotaxis and for the design of systems exploiting magnetotactic bacteria in biomedical applications.

I. INTRODUCTION

Nature has invented an incredible mechanism to lead magnetotactic bacteria such as *Magnetospirillum gryphiswaldense* to its optimum feeding grounds: a compass needle in its cell body in the form of a chain of self-assembled magnetite crystallites, each a few tens of nanometers in diameter [1–3]. Even better than a compass, which only indicates the direction of the earth’s magnetic field, this chain of magnetosomes directly orients the bacterium along the field, as a result of the torque exerted. Using its flagella and a biological sensor for oxygen content [4], the bacterium then propels itself along the magnetic field lines towards sources of nourishment in aquatic sediments. By restricting *M. gryph.*’s motion along one dimension, the chain of magnetosomes increases the efficiency of this search [5, 6].

The discovery of magnetotactic bacteria has inspired a number of ideas for biomedical applications [7–13], including using them as nano-robots with magnetic actuation [14, 15] or as sensing devices [16]. The biomineralization process governing the formation of magnetosome chains is also of great interest for finding new routes of material generation [17]. More exotic research directions include the use of magnetotactic bacteria in waste water treatment [18] or studies linking the presence of magnetite nanoparticles – similar to those making up magnetosomes – in meteorites from Mars to potential presence of ancient life on that planet [19–21].

Precise measurements of the magnetic properties of magnetotactic bacteria, specifically anisotropy and total magnetic moment, are the key to understanding the mechanisms behind magnetotaxis [22–28]. One approach is to monitor the motion of either ensembles or individual bacteria in the presence of magnetic fields [29–33]. Reufer et al. [30] investigated the trajectories of *M. gryph.* swimming in a magnetic field, determining an average magnetic moment of $2 \cdot 10^{-16}$ A m² per bacterium. Zahn et

al. [29] extracted the moment of about 150 bacteria in liquid by tracking and modeling the rotation and translation of individual bacteria under the influence of magnetic tweezers. Typically, however, magnetic properties deduced from such measurements rely on assumptions about the motion of the bacteria in liquid. The magnetic moment of ensembles of magnetotactic bacteria has been measured directly using a superconducting quantum interference device (SQUID) [34, 35]. Individual bacteria have also been studied via magnetic imaging techniques, including X-ray magnetic circular dichroism combined with scanning transmission X-ray microscopy [36–40] and electron holography [41]. In particular, Dunin-Borowski et al. used electron holography to visualize the magnetic stray fields of an individual *Magnetospirillum magnetotacticum* in remanence [41].

None of these techniques, however, yield the magnetic hysteresis of an individual bacterium, from which magnetic properties such as coercivity, anisotropy, and switching behavior can be determined. Knowledge of these properties is especially important for applications involving magnetic actuation or sensing. The challenge of such a measurement is to resolve the tiny magnetic moment of a single chain of magnetosomes. Dynamic cantilever magnetometry (DCM) [42–45], which is a particularly sensitive form of torque magnetometry, provides a method for measuring the magnetism of nanometer-scale magnetic systems. Gysin et al. first used DCM to measure the magnetic hysteresis of an ensemble of about 100 *M. gryph.*, resulting in a magnetic moment of $5 \cdot 10^{-16}$ A m² [46] per bacterium. A few years later, using a more sensitive cantilever, the same group managed to measure the hysteresis of an individual *M. gryph.* [47], however, low signal-to-noise ratio precluded a detailed analysis of the measurements.

By attaching a single *M. gryph.* to an ultrasensitive SiN cantilever, we resolve its magnetic hysteresis via DCM. Furthermore, based on transmission electron microscopy

(TEM) images, we create a micromagnetic model for the bacterium's chain of magnetosomes and compare it to DCM measurements. This comparison allows us to determine the likely progression of the magnetosomes' magnetic configurations as a function of applied field, as well as determining the remanent magnetization, effective anisotropy, and switching field of the bacterium. In measurements of ensembles, these properties of individual bacteria are obscured by inhomogeneity in the size, shape, and orientation of the chains of magnetosomes.

II. DYNAMIC CANTILEVER MAGNETOMETRY

In DCM, as shown in Fig. 1, the sample under investigation is attached to the free end of a cantilever, which is driven into self-oscillation at its fundamental mechanical resonance frequency f . The measurement consists of monitoring changes in this frequency $\Delta f = f - f_0$ as a function of a uniform applied magnetic field \mathbf{H} , where f_0 is the resonance frequency at $H = 0$. Δf reveals the curvature of the magnetic system's free energy with respect to rotations about the cantilever oscillation axis [48, 49]. This quantity can be intuitively understood as an analogue to magnetic susceptibility: while susceptibility quantifies the magnetic response of a sample to changes in the magnitude of \mathbf{H} , Δf quantifies the response to changes in its orientation. Measurements of Δf are particularly useful for identifying magnetic phase transitions [48, 50, 51], as well as providing information on the switching, saturation magnetization, coercivity, and the anisotropy of a magnetic system [52].

The cantilevers used in this measurement are fabricated from SiN and are $55.8\ \mu\text{m}$ long, $1.94\ \mu\text{m}$ wide and $50\ \text{nm}$ thick. The resonance frequency f_0 of the fundamental mechanical mode used for magnetometry is $16.9\ \text{kHz}$ with an effective spring constant of $44\ \mu\text{N/m}$ and quality factor of a few thousand at room temperature. Once the sample has been attached, the cantilever is mounted in a vibration-isolated vacuum chamber at 10^{-6} mbar. Using an external rotatable superconducting magnet, magnetic fields up to $4.5\ \text{T}$ can be applied along any direction spanning 225° in the plane of cantilever oscillation (xz -plane), as specified by the angle θ_h shown in Fig. 1. The cantilever's flexural motion is read out using an optical fiber interferometer using $100\ \text{nW}$ of laser light at $1550\ \text{nm}$ [53]. A piezoelectric actuator mechanically drives the cantilever at f with a constant oscillation amplitude of a few tens of nanometers using a feedback loop implemented by a field-programmable gate array. This process enables the fast and accurate extraction of Δf from the cantilever deflection signal [54].

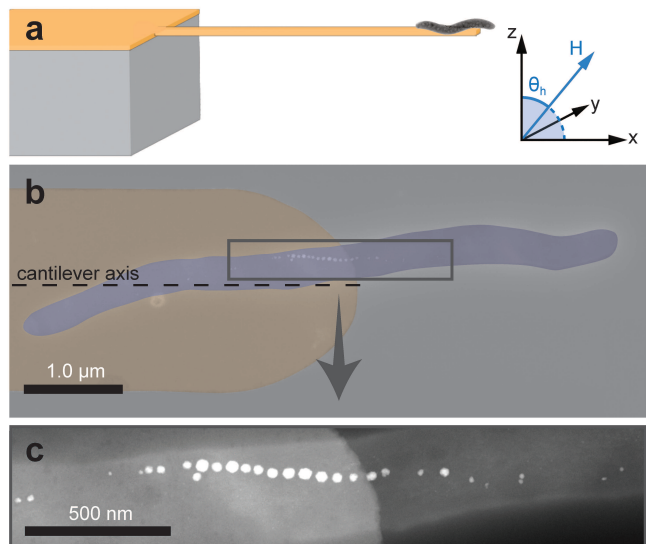


FIG. 1. **Measurement setup and bacterium-on-cantilever probe.** **a** Sketch of a cantilever with a single bacterium attached at the tip and definition of the coordinate axes. **b** False color high-angle annular dark-field scanning transmission electron microscopy image showing the relative orientation of the magnetosome chain with respect to the cantilever axis and **c** a close-up view of the magnetosome chain.

III. SAMPLE PREPARATION

Cells of *M. gryph.* DSM 6361 were grown under anaerobic conditions in sealed Hungate tubes containing $10\ \text{ml}$ of Flask Standard Medium under a headspace of N_2 , as described before [55, 56]. The cells are then fixed with formaldehyde. Next, a droplet of solution containing the cells is placed on the surface of a polytetrafluoroethylene sheet. A small permanent magnet placed under the sheet helps to retain bacteria, which contain magnetosomes. After 10 minutes, the droplet is dried with a gentle flow of compressed air. A micromanipulator system (Narishige) is used to pick up an individual bacterium from the surface, and transfer it to the free end of the ultra-soft cantilever. The bacterium is attached to the apex of the cantilever for magnetic characterization as shown in Fig. 1b, oriented roughly with the cantilever axis using the micromanipulator, and fixed in place with UV glue (Thorlabs).

IV. MEASUREMENTS

We perform two types of DCM measurements just below room temperature at $T \approx 284\ \text{K}$. In the first, shown in Fig. 2, we monitor Δf as a function of the direction θ_h of a large field of constant magnitude $\mu_0 H = 3.5\ \text{T}$ applied in the plane perpendicular to the cantilever's rotation axis (xz -plane). In a magnetic field H large

enough to saturate the system, as in this case, the maxima and minima of $\Delta f(\theta_h)$ indicate the directions of the easy and hard axes, respectively [45, 49]. The data plotted in Fig. 2 show the signatures of uniaxial anisotropy with the maximum and minimum separated by 90° and the maximum indicating the direction of the easy axis, which roughly coincides with the axis of the magnetosome chain.

In the second type of measurement, shown in Fig. 3, we measure Δf as we sweep H along a fixed direction from large positive to large negative values. Analysis of the resulting $\Delta f(H)$ hysteresis measurements allows for the extraction of the remanent magnetic moment as well as information on the system's magnetic switching behavior and the progression of magnetic configurations present as the system reverses. Measurements taken for $\theta_h = 90^\circ$ (along the axis of the magnetosome chain), shown in Fig. 3a and b, and for $\theta_h = 0^\circ$, shown in Fig. 3c and d, show – as expected – the characteristic response of a magnetic system with uniaxial anisotropy with \mathbf{H} applied along its easy and hard axes, respectively [45]. The sharp discontinuity seen in Fig. 3b is the signature of magnetic switching in reverse applied field allowing us to deduce a coercive field of around 20 mT for the chain.

Upon completion of the DCM measurements, the cantilever is transferred to a grid for subsequent high-resolution (HR)TEM and high-angle annular dark-field scanning transmission electron microscopy (HAADF-STEM) imaging. During this process, the cantilever is broken off of its base at its clamping point, making further DCM measurements impossible. Individual magnetite magnetosomes, which are only surrounded by biological tissue, are clearly resolved in the HAADF-STEM images, as shown in Fig. 1b. This image shows the individual bacterium under investigation, which is still attached to the end of the SiN cantilever. The brightest contrast in the image corresponds to the projection of each magnetosome on the xy -plane, allowing for the determination of each particle's position and shape. The image reveals the alignment of the magnetosome chain with the cantilever's long axis. We extract the positions, equivalent ellipse semi-axes, and orientation of the individual magnetosomes in the xy -plane, using color-thresholding and grain detection (Gwyddion). Size and position variations along z cannot be extracted and are assumed to be small. A list of the coordinates and equivalent radius of each magnetosome is given in Ref. 54.

HRTEM images of each individual magnetosome and their Fourier transforms also provide information on their crystallinity and orientation. Crystal planes visible in the images show that at least 25 of the 29 magnetosomes are in a crystalline state. We do not find correlations between the orientation of these planes and either the axis of the chain or the orientation of neighbouring magnetosomes [54]. Experimental circumstances prevented the extraction of the exact crystalline orientation of each magnetosome, which would have provided the orientation of each particle's magneto-crystalline anisotropy axes.

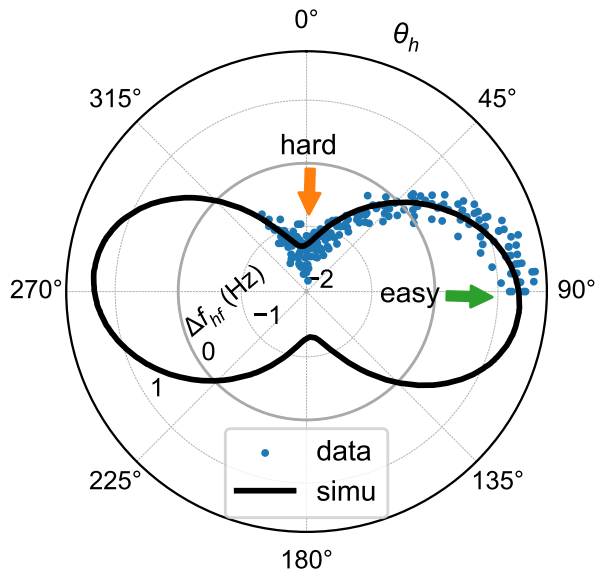


FIG. 2. **DCM field rotation measurement and simulation.** $\Delta f(\theta_h)$ measured at $\mu_0 H = 3.5$ T is plotted as blue points. Orange and green arrows indicate the hard and easy axes, respectively, as derived from simulation, shown in black.

V. ANALYSIS AND DISCUSSION

DCM data plotted in Fig. 2 indicate the presence of a dominant uniaxial anisotropy along the chain of magnetosomes, originating from dipolar interactions between the magnetosomes, similar to shape anisotropy. Detailed consideration, however, reveals the role of other magnetic anisotropies. To deepen our understanding, we construct a micromagnetic model of the magnetosome chain, in which we consider three contributions to the chain's effective magnetic anisotropy: shape anisotropy of the individual particles, cubic magneto-crystalline anisotropy of the individual particles, and the anisotropy arising from dipolar interactions between magnetosomes. Using the position, shape, and orientation of the magnetosomes measured by TEM, as well as material parameters from the literature [57], the model determines their magnetic state resulting from the application of an external magnetic field. By including the geometry of the DCM experiment and the properties of the cantilever, we calculate Δf and use it to iteratively adjust the input parameters, optimizing the agreement between simulated and measured Δf . In this way, features in hysteresis curves of $\Delta f(H)$ such as jumps, dips, or humps can be associated with events such as magnetic switching or collective rotation of magnetic moments.

Our lack of knowledge of the orientation of the crystalline anisotropy axes of the individual magnetosomes and their morphology in the z -direction forces us to fall back on a 'best guess' strategy in order to construct a realistic model. We therefore make two assumptions about their positions and extent along z : 1) we assume that all the magnetosomes lie in the same xy -plane and 2) that

their shapes are ellipsoidal with the z semi-axes set to match the longer in-plane axis. We then simulate 500 iterations of the high-field $\Delta f(\theta_h)$ measurement shown in Fig. 2 with randomly oriented crystalline anisotropy axes for each magnetosome. The parameters from the 20 best matches are then used to simulate the $\Delta f(H)$ hysteresis measurements shown in Fig. 3 for a number of magnetic field orientations close to the experimental orientations. Further details on the simulations can be found in Ref. 54.

One set of parameters is found to provide the best match to the measurements, coinciding with both the experimental $\Delta f(\theta_h)$ and $\Delta f(H)$ data within the measurement noise, as shown in Figs. 2 and 3. The model yields an effective easy-axis anisotropy of the chain as a whole, containing all contributions from shape and crystalline anisotropy of the individual magnetosomes as well as dipolar interactions. Expressed in units of crystalline anisotropy we find an effective anisotropy constant of 13.8 kJ/m^3 , which is similar to the value of the crystalline anisotropy itself. Typically, in literature [2], only a minimal magnetic moment for effective magnetotaxis is given. The effective anisotropy of the magnetosome chain is, however, an equally important quantity, because it quantifies the stability of the magnetic moment along the chain axis against perturbation.

It is interesting to note that most of the 500 simulated high-field rotation curves do not show the characteristic shape resulting from simple uniaxial magnetic anisotropy along the chain direction, as measured for this bacterium in Fig. 2. Rather, they show a more complex angular dependence with signatures of the shape and randomly oriented crystalline anisotropies of the individual magnetosomes, as shown in Ref. 54. This finding highlights that anisotropies of the individual magnetosomes should not be neglected and suggests that the absence of features due to these anisotropies in our measurement is likely a coincidence due to the specific orientations of the magnetosomes in this chain. Nevertheless, even in iterations, in which the orientations of the individual magnetosomes result in more complex $\Delta f(\theta_h)$, the dominant easy axis is always set by the direction of the magnetosome chain. The fact that the chain axis sets the global energetic minimum of the magnetic anisotropy energy, despite the competing anisotropies of individual magnetosomes, ultimately ensures that every bacterium's body aligns along magnetic field lines.

Some previous studies report the alignment of a $\langle 111 \rangle$ -type axis of individual magnetosomes with the chain axis for several different types of magnetotactic bacteria [58–61], including *M. gryph*. We tested the consistency of our measurements with such an alignment, by simulating a number of random orientations in which each magnetosome had a $\langle 111 \rangle$ -type axis pinned along the chain direction. Under this constraint, no match to the measurements was found, with an exemplary result shown in Ref. 54. In fact, averaged over all magnetosomes, the simulation with the best match has an angle between the

chain axis and the nearest $\langle 111 \rangle$ -type axis of 27° with a standard deviation of 11° . We therefore conclude that no specific alignment of the $\langle 111 \rangle$ axes with the chain axis is present in the measured bacterium.

Measurements of the hysteresis of $\Delta f(H)$, shown in Fig. 3, are taken with \mathbf{H} aligned along the magnetic easy and hard directions, as determined by the measurements shown in Fig. 2. In the limit of low fields, the remanent magnetic moment can be directly determined from $\Delta f(H)$ with the knowledge of the cantilever properties [45]. We find $(1.84 \pm 0.54) \cdot 10^{-16} \text{ A m}^2$ after \mathbf{H} is applied parallel to the chain axis, and, astonishingly, an order of magnitude less, $(0.26 \pm 0.14) \cdot 10^{-16} \text{ A m}^2$, after \mathbf{H} is applied perpendicular to the chain axis. These numbers are closely reproduced by our best-scenario micromagnetic model, for which the calculated $\Delta f(H)$ is also shown in Fig. 3. The saturation magnetic moment within the model is $1.93 \cdot 10^{-16} \text{ A m}^2$. Therefore, almost the full moment is preserved in remanence after \mathbf{H} is applied parallel to the chain axis, while it nearly vanishes after the application of perpendicular fields. The magnitude of the saturation moment is in very good agreement with the previous measurements based on optical microscopy [29, 30] and DCM [46].

The reasons for the large difference in remanent moment after the application of parallel and perpendicular fields can be deduced from a detailed analysis of the measured and simulated $\Delta f(H)$ shown in Fig. 3. In the measurement with the field applied along the easy-axis, shown in Fig. 3b, $\Delta f(H)$ monotonically decreases from high fields down to zero. In a reverse field of -17 mT , a jump occurs and thereafter the curve progresses symmetrically as for positive fields. Such behavior and the V-shape of the curve can be explained via a single macrospin approximation [45]: all magnetic moments are all aligned with the external field, coinciding with the easy-axis of the effective magnetic anisotropy and, shortly after field reversal, collectively flip their direction in a single switching event. Simulations reveal that this picture conceals a more complex behavior: as the applied field is swept from saturation down towards zero, magnetosomes at the ends of the chain reorient the alignment of their magnetic moments from coinciding with the chain axis to coinciding with one of their local magnetic easy-axes. A feature in Δf associated with such a switching event is visible in the simulated $\Delta f(H)$ around 40 mT . To illustrate the result of these switching events, Fig. 4a shows m_x and m_z of the remanent state of the magnetosome chain, where only the main part of the chain maintains alignment of the magnetic moments with the overall magnetic easy axis. Although the noise level of the measurement does not allow for the confirmation of such events in the measured $\Delta f(H)$, the slightly reduced remanent magnetic moment compared to the saturation moment is their direct experimental consequence. Simulations show that further sweeping H in the reverse field direction results in the full magnetic reversal of the chain via switching events of individual or a few magnetosomes,

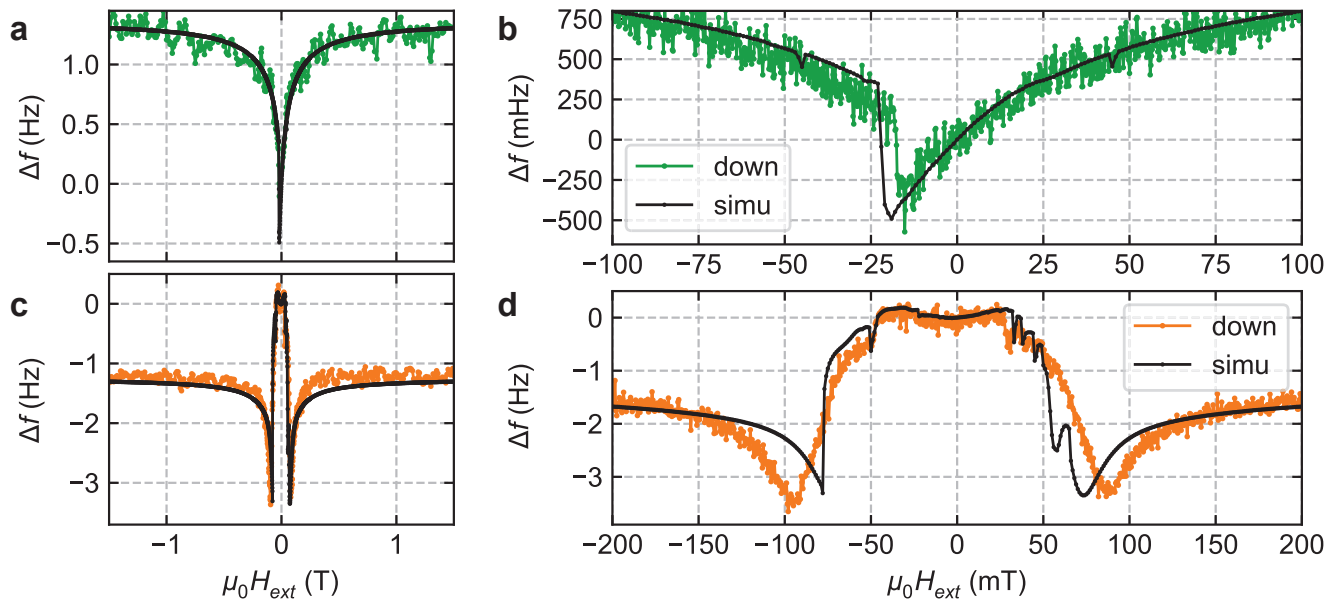


FIG. 3. **DCM hysteresis as a function of applied field.** **a** and **b** Measured $\Delta f(H)$ with \mathbf{H} parallel to the magnetic easy axis plotted in green for a wide and narrow field range, respectively. **c** and **d** Measured $\Delta f(H)$ with \mathbf{H} perpendicular to the magnetic easy axis plotted in orange, for a wide and narrow field range, respectively. In all plots, the applied field $\mu_0 H_{ext}$ is swept from large positive values, through zero, to large negative values. Best-fit simulations are plotted in black.

as illustrated in Fig. 4b.

When H is applied along the magnetic hard-axis, the form of the measured $\Delta f(H)$ is consistent with a gradual rotation of all magnetic moments from alignment with \mathbf{H} towards the easy-axis for decreasing H and back toward the saturation in reverse field (cf. Fig. 9 in Ref. 45). Deviations from this simple behavior appear in the discontinuities at 28 mT and -48 mT in the measured $\Delta f(H)$. The micromagnetic simulations, which reproduce these distinctive features at nearly the same fields of 33 mT and -50 mT, suggest a surprising remanent state, as shown in Fig. 4c. In this state, the magnetic moments on the left half of the chain orient their moments towards the left ($-\hat{x}$), while those on the right orient towards the right ($+\hat{x}$). Together the moments compensate each other, explaining the very low remanent moment compared to the case for which \mathbf{H} is applied along the easy-axis. The first discontinuity around 33 mT is connected to a single magnetosome in the right half of the chain reorienting its magnetization, while the second around 50 mT corresponds to a switch of a full section of magnetosomes aligned with $+\hat{x}$ towards $-\hat{x}$, cf. Fig. 4d and e, respectively. Other bumps in the simulation are connected to switching of either remote magnetosomes or magnetosomes in the two different parts of the chain; more details can be found in the supplementary videos [54]. These events are either hidden in the noise of the measurement or the progression of the magnetic moments takes place slightly differently than in our best-guess simulation.

As the progressions of the chain's magnetic configuration for the two different orientations of the external

field show, the total magnetic moment at remanence depends strongly on the magnetic history of the chain. This dependence is a result of the relatively weak effective anisotropy, which fails to stabilize the magnetic moment in direction of the easy axis against the application of perpendicular fields larger than several tens of millitesla. Nevertheless, because in its natural habitat *M. gryph.* likely never experiences magnetic fields of this magnitude, this effective anisotropy is sufficient to stabilize its magnetic moment in direction of the magnetosome chain and ensure magnetotaxis. Knowledge of the magnetic behavior for field magnitudes beyond earth's magnetic field may become decisive for applications of magnetotactic bacteria such as biological micro-robots, in which stronger fields are typically used.

VI. CONCLUSION

Via ultrasensitive torque magnetometry, combined with transmission electron microscopy and micromagnetic simulations, we determine the remanent magnetic moment of $(1.84 \pm 0.54) \cdot 10^{-16}$ A m² and a saturation moment of $1.93 \cdot 10^{-16}$ A m² of an individual *M. gryph.* cell. Furthermore, we determine an effective easy-axis anisotropy of 13.8 kJ/m³ aligned along the bacterium's chain of magnetosomes. Analysis of the magnetic hysteresis shows that this anisotropy is strong enough to stabilize the remanent magnetic moment in earth's magnetic field. Future experiments, making use of TEM tomography and diffraction to reveal the full morphology

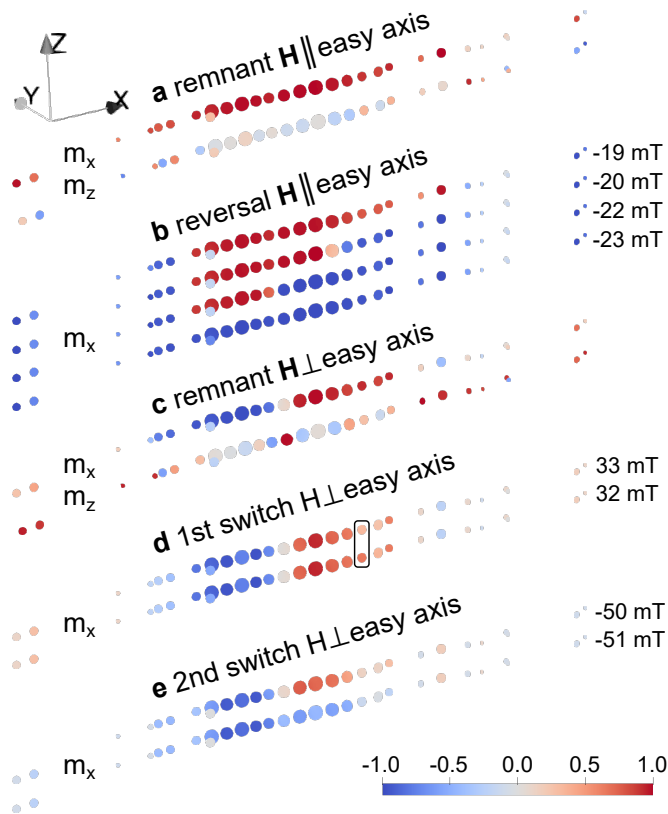


FIG. 4. Visualization of simulated magnetic states of the magnetosome chain. The color bar applies to the component of the magnetization as indicated on the left of each of the visualisations.

and crystal structure of the magnetosomes [59], may allow for higher precision determination of the exact magnetic states of a single bacterium. Improved cantilever sensors could also enable the resolution of the switching of individual magnetosomes, further deepening our understanding of the magnetic reversal process. DCM Measurements of many more individual bacteria would also help to determine the homogeneity of saturation moment, remanent moment, and anisotropy across a population of bacteria.

VII. DATA AVAILABILITY

The data supporting the findings of this study are available on the Zenodo repository at <https://doi.org/10.5281/zenodo.10730902>.

VIII. ACKNOWLEDGMENTS

The authors thank Sascha Martin and his team in the machine shop of the Department of Physics at the University of Basel for help building the measurement system, and the Nano Imaging Lab of the Swiss Nanoscience Institute for their support in taking TEM data. They acknowledge support from the Canton Aargau and the Swiss Nanoscience Institute's PhD program (Project P2107). Calculations were performed at sci-CORE (<http://scicore.unibas.ch/>) scientific computing center at University of Basel.

- [1] R. Uebe and D. Schüler, Magnetosome biogenesis in magnetotactic bacteria, *Nature Reviews Microbiology* **14**, 621 (2016).
- [2] D. Faivre and D. Schüler, Magnetotactic Bacteria and Magnetosomes, *Chemical Reviews* **108**, 4875 (2008).
- [3] C. T. Lefèvre and D. A. Bazylinski, Ecology, Diversity, and Evolution of Magnetotactic Bacteria, *Microbiology and Molecular Biology Reviews* **77**, 497 (2013).
- [4] F. Popp, J. P. Armitage, and D. Schüler, Polarity of bacterial magnetotaxis is controlled by aerotaxis through a common sensory pathway, *Nature Communications* **5**, 5398 (2014).
- [5] R. B. Frankel, D. A. Bazylinski, M. S. Johnson, and B. L. Taylor, Magneto-aerotaxis in marine coccoid bacteria, *Biophysical Journal* **73**, 994 (2018).
- [6] D. Schüler, The biomineralization of magnetosomes in *Magnetospirillum gryphiswaldense*, *International Microbiology* **5**, 209 (2002).
- [7] E. AlphanDéry, I. Chebbi, F. Guyot, and M. Durand-Dubief, Use of bacterial magnetosomes in the magnetic hyperthermia treatment of tumours: A review, *International Journal of Hyperthermia* **29**, 801 (2013).
- [8] D. Serantes, K. Simeonidis, M. Angelakeris, O. Chubykalo-Fesenko, M. Marciello, M. d. P. Morales, D. Baldomir, and C. Martinez-Boubeta, Multiplying Magnetic Hyperthermia Response by Nanoparticle Assembling, *The Journal of Physical Chemistry C* **118**, 5927 (2014).
- [9] O. Felfoul, M. Mohammadi, S. Taherkhani, D. de Lanauze, Y. Zhong Xu, D. Loghin, S. Essa, S. Jancik, D. Houle, M. Lafleur, L. Gaboury, M. Tabrizian, N. Kaou, M. Atkin, T. Vuong, G. Batist, N. Beauchemin, D. Radzioch, and S. Martel, Magneto-aerotactic bacteria deliver drug-containing nanoliposomes to tumour hypoxic regions, *Nature Nanotechnology* **11**, 941 (2016).
- [10] D. Ghosh, Y. Lee, S. Thomas, A. G. Kohli, D. S. Yun, A. M. Belcher, and K. A. Kelly, M13-templated magnetic nanoparticles for targeted in vivo imaging of prostate cancer, *Nature Nanotechnology* **7**, 677 (2012).
- [11] D. Gandia, L. Gandarias, I. Rodrigo, J. Robles-García, R. Das, E. Garaió, J. A. García, M.-H. Phan, H. Srikanth, I. Orue, J. Alonso, A. Muela, and M. L. Fernández-Gubieda, Unlocking the Potential of Magnetotactic Bacteria as Magnetic Hyperthermia Agents, *Small* **15**, 1902626 (2019).
- [12] A. Kraupner, D. Eberbeck, D. Heinke, R. Uebe, D. Schüler, and A. Briel, Bacterial magnetosomes – nature's powerful contribution to MPI tracer research,

- Nanoscale **9**, 5788 (2017).
- [13] F. Mickoleit, C. Lanzloth, and D. Schüler, A Versatile Toolkit for Controllable and Highly Selective Multifunctionalization of Bacterial Magnetic Nanoparticles, *Small* **16**, 1906922 (2020).
- [14] I. S. M. Khalil and S. Misra, Chapter 4 - Control of magnetotactic bacteria, in *Microbiorobotics (Second Edition)*, Micro and Nano Technologies, edited by M. Kim, A. A. Julius, and U. K. Cheang (Elsevier, Boston, 2017) pp. 61–79.
- [15] S. R. Mishra, M. D. Dickey, O. D. Velev, and J. B. Tracy, Selective and directional actuation of elastomer films using chained magnetic nanoparticles, *Nanoscale* **8**, 1309 (2016).
- [16] X. Jiang, J. Feng, L. Huang, Y. Wu, B. Su, W. Yang, L. Mai, and L. Jiang, Bioinspired 1D Superparamagnetic Magnetite Arrays with Magnetic Field Perception, *Advanced Materials* **28**, 6952 (2016).
- [17] D. Schüler, Genetics and cell biology of magnetosome formation in magnetotactic bacteria, *FEMS Microbiology Reviews* **32**, 654 (2008).
- [18] H. Zheng, B. Pang, S. Li, S. Ma, J. Xu, Y. Wen, and J. Tian, Construction of Recombinant Magnetospirillum Strains for Nitrate Removal from Wastewater Based on Magnetic Adsorption, *Processes* **10**, 591 (2022).
- [19] B. Arató, Z. Szányi, C. Flies, D. Schüler, R. B. Frankel, P. R. Buseck, and M. Pósfai, Crystal-size and shape distributions of magnetite from uncultured magnetotactic bacteria as a potential biomarker, *American Mineralogist* **90**, 1233 (2005).
- [20] K. L. Thomas-Keperta, S. J. Clemett, D. A. Bazylinski, J. L. Kirschvink, D. S. McKay, S. J. Wentworth, H. Vali, E. K. Gibson, and C. S. Romanek, Magnetofossils from Ancient Mars: a Robust Biosignature in the Martian Meteorite ALH84001, *Applied and Environmental Microbiology* **68**, 3663 (2002).
- [21] R. B. Frankel and P. R. Buseck, Magnetite biomineralization and ancient life on Mars, *Current Opinion in Chemical Biology* **4**, 171 (2000).
- [22] R. B. Frankel, Magnetic Guidance of Organisms, *Annual Review of Biophysics and Bioengineering* **13**, 85 (1984).
- [23] A. Kalmijn, Biophysics of geomagnetic field detection, *IEEE Transactions on Magnetics* **17**, 1113 (1981).
- [24] X. Zhu, X. Ge, N. Li, L.-F. Wu, C. Luo, Q. Ouyang, Y. Tu, and G. Chen, Angle sensing in magnetotaxis of Magnetospirillum magneticum AMB-1, *Integrative Biology* **6**, 706 (2014).
- [25] S. Klumpp and D. Faivre, Magnetotactic bacteria, *The European Physical Journal Special Topics* **225**, 2173 (2016).
- [26] S. Klumpp, C. T. Lefèvre, M. Bennet, and D. Faivre, Swimming with magnets: From biological organisms to synthetic devices, *Physics Reports Swimming with magnets: From biological organisms to synthetic devices*, **789**, 1 (2019).
- [27] S. Mohammadjad, D. Faivre, and S. Klumpp, Stokesian dynamics simulations of a magnetotactic bacterium, *The European Physical Journal E* **44**, 40 (2021).
- [28] A. Codutti, M. A. Charsooghi, E. Cerdá-Doñate, H. M. Taïeb, T. Robinson, D. Faivre, and S. Klumpp, Interplay of surface interaction and magnetic torque in single-cell motion of magnetotactic bacteria in microfluidic confinement, *eLife* **11**, e71527 (2022).
- [29] C. Zahn, S. Keller, M. Toro-Nahuelpan, P. Dorscht, W. Gross, M. Laumann, S. Gekle, W. Zimmermann, D. Schüler, and H. Kress, Measurement of the magnetic moment of single Magnetospirillum gryphiswaldense cells by magnetic tweezers, *Scientific Reports* **7**, 3558 (2017).
- [30] M. Reufer, R. Besseling, J. Schwarz-Linek, V. A. Martinez, A. N. Morozov, J. Arlt, D. Trubitsyn, F. B. Ward, and W. C. K. Poon, Switching of Swimming Modes in Magnetospirillum gryphiswaldense, *Biophysical Journal* **106**, 37 (2014).
- [31] D. Le Sage, K. Arai, D. R. Glenn, S. J. DeVience, L. M. Pham, L. Rahn-Lee, M. D. Lukin, A. Yacoby, A. Komeili, and R. L. Walsworth, Optical magnetic imaging of living cells, *Nature* **496**, 486 (2013).
- [32] R. Nadkarni, S. Barkley, and C. Fradin, A Comparison of Methods to Measure the Magnetic Moment of Magnetotactic Bacteria through Analysis of Their Trajectories in External Magnetic Fields, *PLOS ONE* **8**, e82064 (2013).
- [33] A. Bahaj, P. James, and F. Moeschler, An alternative method for the estimation of the magnetic moment of non-spherical magnetotactic bacteria, *IEEE Transactions on Magnetics* **32**, 5133 (1996).
- [34] Y. R. Chemla, H. L. Grossman, T. S. Lee, J. Clarke, M. Adamkiewicz, and B. B. Buchanan, A New Study of Bacterial Motion: Superconducting Quantum Interference Device Microscopy of Magnetotactic Bacteria, *Biophysical Journal* **76**, 3323 (1999).
- [35] R. Prozorov, T. Prozorov, S. K. Mallapragada, B. Narasimhan, T. J. Williams, and D. A. Bazylinski, Magnetic irreversibility and the Verwey transition in nanocrystalline bacterial magnetite, *Physical Review B* **76**, 054406 (2007).
- [36] K. P. Lam, A. P. Hitchcock, M. Obst, J. R. Lawrence, G. D. W. Swerhone, G. G. Leppard, T. Tyliczszak, C. Karunakaran, J. Wang, K. Kaznatcheev, D. A. Bazylinski, and U. Lins, Characterizing magnetism of individual magnetosomes by X-ray magnetic circular dichroism in a scanning transmission X-ray microscope, *Chemical Geology* **270**, 110 (2010).
- [37] L. Marcano, I. n. Orue, D. Gandia, L. Gandarias, M. Weigand, R. M. Abrudan, A. García-Prieto, A. García-Arribas, A. Muela, M. L. Fernández-Gubieda, and S. Valencia, Magnetic Anisotropy of Individual Nanomagnets Embedded in Biological Systems Determined by Axi-asymmetric X-ray Transmission Microscopy, *ACS Nano* **16**, 7398 (2022).
- [38] S. S. Kalirai, K. P. Lam, D. A. Bazylinski, U. Lins, and A. P. Hitchcock, Examining the chemistry and magnetism of magnetotactic bacterium *Candidatus Magnetovibrio blakemorei* strain MV-1 using scanning transmission X-ray microscopy, *Chemical Geology* **300-301**, 14 (2012).
- [39] S. S. Kalirai, D. A. Bazylinski, and A. P. Hitchcock, Anomalous Magnetic Orientations of Magnetosome Chains in a Magnetotactic Bacterium: Magnetovibrio blakemorei Strain MV-1, *PLOS ONE* **8**, e53368 (2013).
- [40] S. Staniland, B. Ward, A. Harrison, G. van der Laan, and N. Telling, Rapid magnetosome formation shown by real-time x-ray magnetic circular dichroism, *Proceedings of the National Academy of Sciences* **104**, 19524 (2007).
- [41] R. E. Dunin-Borkowski, M. R. McCartney, R. B. Frankel, D. A. Bazylinski, M. Pósfai, and P. R. Buseck, Magnetic Microstructure of Magnetotactic Bacteria by Electron Holography, *Science* **282**, 1868 (1998).

- [42] C. Rossel, P. Bauer, D. Zech, J. Hofer, M. Willemin, and H. Keller, Active microlevers as miniature torque magnetometers, *Journal of Applied Physics* **79**, 8166 (1996).
- [43] J. G. E. Harris, D. D. Awschalom, F. Matsukura, H. Ohno, K. D. Maranowski, and A. C. Gossard, Integrated micromechanical cantilever magnetometry of Ga_{1-x}Mn_xAs, *Applied Physics Letters* **75**, 1140 (1999).
- [44] B. C. Stipe, H. J. Mamin, T. D. Stowe, T. W. Kenny, and D. Rugar, Magnetic Dissipation and Fluctuations in Individual Nanomagnets Measured by Ultrasensitive Cantilever Magnetometry, *Physical Review Letters* **86**, 2874 (2001).
- [45] B. Gross, D. P. Weber, D. Ruffer, A. Buchter, F. Heimbach, A. Fontcuberta i Morral, D. Grundler, and M. Poggio, Dynamic cantilever magnetometry of individual CoFeB nanotubes, *Physical Review B* **93**, 064409 (2016).
- [46] U. Gysin, S. Rast, A. Aste, T. Speliotis, C. Werle, and E. Meyer, Magnetic properties of nanomagnetic and bi-magnetic systems analyzed using cantilever magnetometry, *Nanotechnology* **22**, 285715 (2011).
- [47] M. Wasem, *Atomic Force Microscopy of Nanoparticles and Biological Cells*, Thesis, University of Basel (2015).
- [48] K. A. Modic, M. D. Bachmann, B. J. Ramshaw, F. Arnold, K. R. Shirer, A. Estry, J. B. Betts, N. J. Ghimire, E. D. Bauer, M. Schmidt, M. Baenitz, E. Svanidze, R. D. McDonald, A. Shekhter, and P. J. W. Moll, Resonant torsion magnetometry in anisotropic quantum materials, *Nature Communications* **9**, 3975 (2018).
- [49] B. Gross, S. Philipp, E. Josten, J. Leliaert, E. Wetterskog, L. Bergström, and M. Poggio, Magnetic anisotropy of individual maghemite mesocrystals, *Physical Review B* **103**, 014402 (2021).
- [50] A. Mehlin, F. Xue, D. Liang, H. F. Du, M. J. Stolt, S. Jin, M. L. Tian, and M. Poggio, Stabilized Skyrmion Phase Detected in MnSi Nanowires by Dynamic Cantilever Magnetometry, *Nano Letters* **15**, 4839 (2015).
- [51] B. Gross, S. Philipp, K. Geirhos, A. Mehlin, S. Bordács, V. Tsurkan, A. Leonov, I. Kézsmárki, and M. Poggio, Stability of Néel-type skyrmion lattice against oblique magnetic fields in GaV₄S₈ and GaV₄Se₈, *Physical Review B* **102**, 104407 (2020).
- [52] S. Philipp, B. Gross, M. Reginka, M. Merkel, M. M. Claus, M. Sulliger, A. Ehresmann, and M. Poggio, Magnetic hysteresis of individual Janus particles with hemispherical exchange biased caps, *Applied Physics Letters* **119**, 222406 (2021).
- [53] D. Rugar, Improved fiber-optic interferometer for atomic force microscopy, *Applied Physics Letters* **55**, 2588 (1989).
- [54] See Supplemental Material [url] for further information.
- [55] U. Heyen and D. Schüler, Growth and magnetosome formation by microaerophilic *Magnetospirillum* strains in an oxygen-controlled fermentor, *Applied Microbiology and Biotechnology* **61**, 536 (2003).
- [56] Y. Li, E. Katzmann, S. Borg, and D. Schüler, The Periplasmic Nitrate Reductase Nap Is Required for Anaerobic Growth and Involved in Redox Control of Magnetite Biomineralization in *Magnetospirillum gryphiswaldense*, *Journal of Bacteriology* **194**, 4847 (2012).
- [57] P. Ó Conbhuí, W. Williams, K. Fabian, P. Ridley, L. Nagy, and A. R. Muxworthy, MERRILL: Micromagnetic Earth Related Robust Interpreted Language Laboratory, *Geochemistry, Geophysics, Geosystems* **19**, 1080 (2018).
- [58] D. Gandia, L. Gandarias, L. Marcano, I. n. Orue, D. Gil-Cartón, J. Alonso, A. García-Arribas, A. Muela, and M. L. Fernández-Gubieda, Elucidating the role of shape anisotropy in faceted magnetic nanoparticles using biogenic magnetosomes as a model, *Nanoscale* **12**, 16081 (2020).
- [59] I. Orue, L. Marcano, P. Bender, A. García-Prieto, S. Valencia, M. A. Mawass, D. Gil-Cartón, D. A. Venero, D. Honecker, A. García-Arribas, L. F. Barquín, A. Muela, and M. L. Fernández-Gubieda, Configuration of the magnetosome chain: a natural magnetic nanoarchitecture, *Nanoscale* **10**, 7407 (2018).
- [60] A. Körnig, M. Winklhofer, J. Baumgartner, T. P. Gonzalez, P. Fratzl, and D. Faivre, Magnetite Crystal Orientation in Magnetosome Chains, *Advanced Functional Materials* **24**, 3926 (2014).
- [61] S. Mann, R. B. Frankel, and R. P. Blakemore, Structure, morphology and crystal growth of bacterial magnetite, *Nature* **310**, 405 (1984).

SUPPLEMENTAL MATERIAL

A. Data Acquisition and Processing

Sampling time for the frequency data varies between 1 and 5 s, mostly limited by a spurious time-dependent frequency drift, which adds to the magnetic contribution,

$$f = f_0 + f_{\text{magnetic}}(H) + f_{\text{drift}}(t).$$

The drift likely originates from liquid evaporating from the bacterial cell into the surrounding vacuum. This mechanism is supported by the observation that f increases monotonically over time at room temperature (the expected effect of a loss of mass on the cantilever), while no drift is observed at cryogenic temperatures, when the sample is frozen. We approximate $f_{\text{drift}}(t)$ to be linear in time and subtract it from f . For hysteresis measurements of the resonant frequency as function of applied field, $f(H)$, f_0 is the average of $f(0)$ for down- and up-sweep, and for high field rotational measurements it is determined separately. Noise and oversampling are reduced by applying a rolling mean with a window of size ≤ 3 data points. Note that the measurements at hand are close to the thermal limit of what is possible with the given setup and cantilevers. Specifically, the cantilever's mechanical dissipation has to be further reduced in order to increase the signal-to-noise ratio, so that further details of the magnetic hysteresis can be resolved.

For the error estimation of the remanent magnetic moment we assume a 5 % error for both spring constant k_0 and effective length l_e of the cantilever, both of which rely on knowledge of the exact cantilever geometry. This geometry is estimated from SEM images and goes into COMSOL simulations determining k_0 and l_e . From experience, we know that error is typically below 5 %. The error in the external magnetic field is assumed to be given by earth's magnetic field.

B. Cantilever properties

The cantilever is commercially available (Nunano) and made of SiN. Its lateral dimensions are measured using scanning electron microscopy, it is 1.94 μm wide and 55.8 μm long. Its nominal thickness is 50 nm. The experimentally observed resonance frequencies of the bacterium-loaded cantilever at zero field are $f_0 = 16.9$ kHz and $f_1 = 104.9$ kHz, where f_1 is the frequency of the first harmonic. We use the *Comsol Multiphysics* software package to construct a finite element model of the cantilever, and adjust its properties so that its calculated resonance frequencies match the measured frequencies. The Young's modulus of SiN is set to 250 GPa, its density to 3100 kg/m³ and Poisson's ratio to 0.23. The bacterium is modeled as a 5 μm long bar with flat bottom and rounded top. Its width is 300 nm and its density is assumed to be the same as for water ($\rho = 1000$ kg/m³). In order to match f_0 and f_1 , a small, linear gradient in the thickness of the cantilever is introduced, such that it is thickest at its base (39.9 nm) and becomes thinner towards the tip (38.2 nm). Using this model, we calculate an effective length $l_{\text{eff}} = 39.4$ μm and a spring constant $k_0 = 44$ $\mu\text{N/m}$ for the cantilever, which are used to calculate the magnetic quantities as discussed in the main text.

C. Micromagnetic simulations

Micromagnetic simulations are performed with the finite-difference software package *MuMax*³. Material parameters are taken from literature [1]: we set the exchange stiffness to $A_{ex} = 13.5$ pJm, the saturation magnetization to $M_s = 483.9$ kA/m, and the first order cubic anisotropy constant to $K_{c1} = -14.0$ kJ/m³.

As discussed in the main text, size, position and orientation of the individual magnetosomes in the xy -plane are taken from transmission electron microscopy (TEM) data. We extrapolate the z dimension in three different scenarios: (1) spherical magnetosomes without shape anisotropy, (2) ellipsoidal magnetosomes with the z semi-axes set to an average of the inplane axes or (3) the longer inplane axis. The volume of the magnetosomes is scaled by a factor of 0.875 to match the high field asymptotes of the measurement. Given the lack of knowledge on the full morphology of the magnetosomes this seems to be a reasonable deviation. The orientation of the cubic anisotropy axes is randomly chosen for each magnetosome. A list of all magnetosomes and their properties is given below.

The final, best matching set of simulations presented in the main text is chosen via an iterative process. We start by finding the 20 best matches for the high field rotation data from 500 repetitions with different sets of randomly oriented cubic anisotropy axes (see Fig. 2 in the main text). Then about five hysteresis curves are simulated for alignment of the external field matching and slightly deviating from both easy and hard magnetic directions, respectively. This is done because many features in the simulations depend sensitively on this alignment. Then, the set of best matching simulations is chosen by eye, trying to obtain the best overall match in both high and low fields. The best set is taken

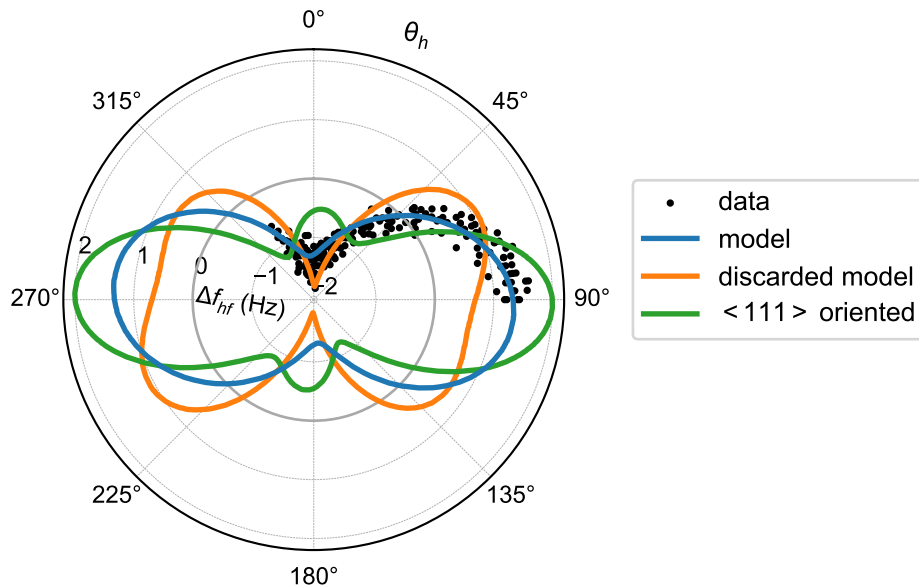


FIG. S1. **DCM field rotation measurement and simulations.** $\Delta f_{hf}(\theta_h)$ measured at $\mu_0 H = 3.5$ T plotted along with various simulations with different combinations of orientations for each magnetosome's anisotropy axes.

from scenario (3), but also for the other scenarios only slightly worse matching is found. To illustrate the effect of different combinations of orientations of the anisotropy axes of the magnetosomes, in Fig. S1, we plot the high field rotation data for the best and a bad with the experiment. Furthermore, a set of data is shown for which one of the $\langle 111 \rangle$ -type axes for each magnetosome is aligned with the chain axis.

D. List of magnetosomes and transmission electron microscopy images

High resolution (HR)TEM images of all magnetosomes are shown in Tabs. S2 and S3. For many of the images, crystal planes are visible, e.g. images 3 and 4 in Tab. S2. Some only show indications of crystal planes in the fast Fourier transform. A full list of these findings is given in Tab. S1. The orientation of the crystal planes differ from image to image, but experimental conditions did not allow for the extraction of the exact orientations of the magnetosomes' crystal structures in space.

[1] Ó Conbhuí, P. *et al.* MERRILL: Micromagnetic Earth Related Robust Interpreted Language Laboratory. *Geochemistry, Geophysics, Geosystems* **19**, 1080–1106 (2018).

No	x (nm)	y (nm)	r_{eq} (nm)	a (nm)	b (nm)	ϕ_a ($^\circ$)	cp
1	15	152	10	11	9	-10	n
2	66	145	12	12	11	25	y (fft)
3	341	51	6	6	5	-51	y
4	444	46	7	8	6	-36	y
5	470	39	12	13	11	-39	y
6	508	39	12	13	12	-24	y
7	597	24	13	14	12	-9	n
8	629	61	14	15	13	31	y
9	647	26	22	22	21	26	y
10	695	31	18	20	17	-29	y (fft)
11	745	30	22	22	21	2	y
12	791	34	16	18	15	-14	y (fft)
13	832	38	17	17	16	-14	y
14	880	48	18	19	18	-14	y
15	934	48	21	22	19	11	y (fft)
16	988	50	22	24	20	3	y (fft)
17	1042	58	20	21	19	-27	y (fft)
18	1094	61	18	19	17	72	y
19	1148	58	14	15	14	32	y
20	1209	55	15	17	13	27	y
21	1256	42	12	13	11	-12	y
22	1375	42	10	11	9	51	n
23	1454	39	15	16	14	-16	y
24	1543	60	9	10	8	-85	y
25	1590	73	6	7	5	78	y (fft)
26	1701	60	7	7	7	-18	n
27	1705	44	8	9	8	83	y (fft)
28	1990	51	9	12	7	4	y
29	2050	17	7	7	6	25	y

TABLE S1. **List of magnetosomes and their properties.** x and y are the center of mass coordinates (assuming constant density), r_{eq} the equivalent radius of a circle with the same area as determined via image processing, a and b are the semi-axes of an equivalent ellipse, ϕ_a the inplane orientation angle of a , and cp stands for crystal plane, indicating, if crystal planes are visible via TEM. y = yes, n = no and (fft) signifies that the crystal planes are only visible via fast Fourier transform.

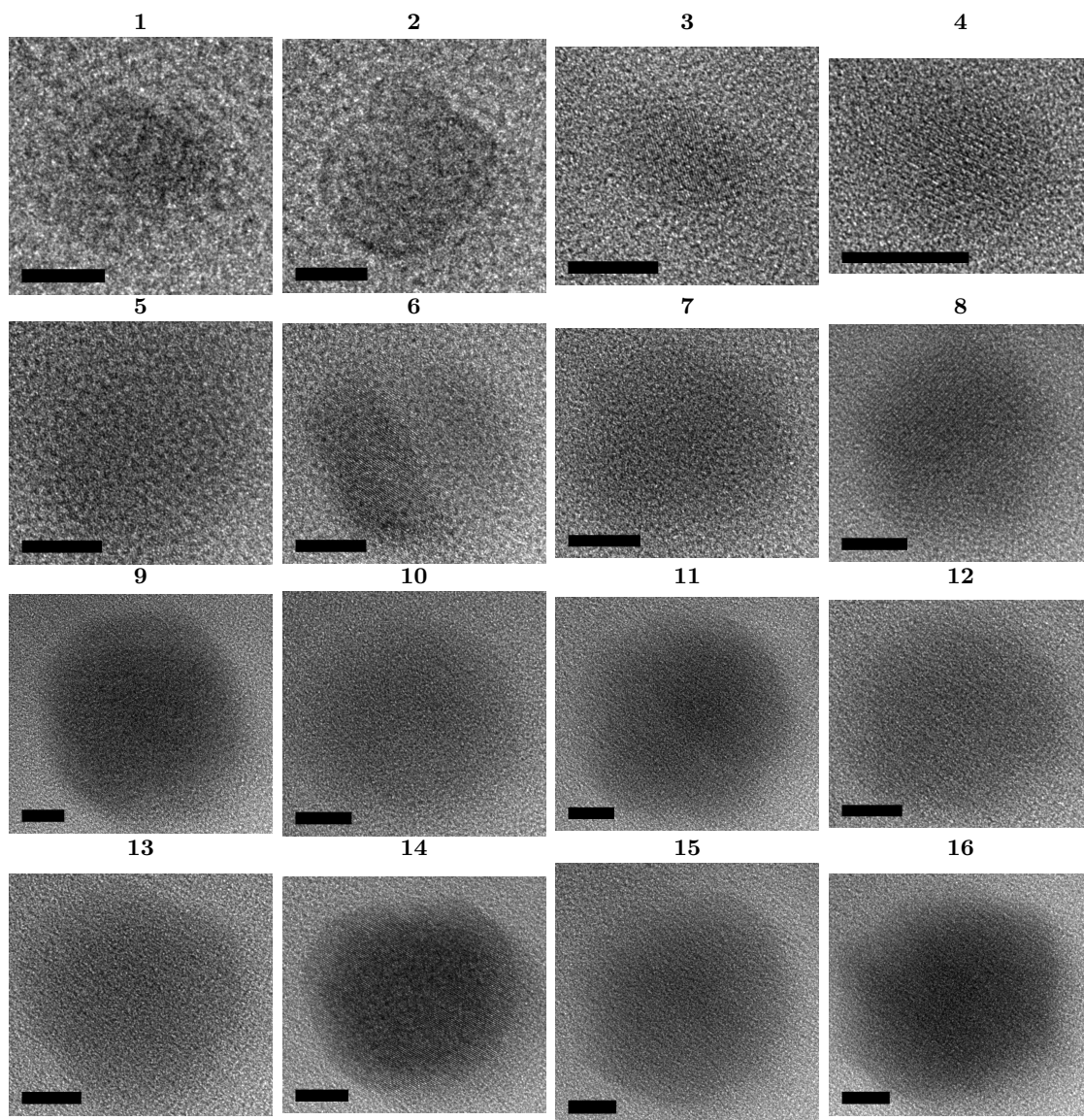


TABLE S2. HRTEM images of the individual magnetosomes 1-16. The scale bar in the images is 5 nm.

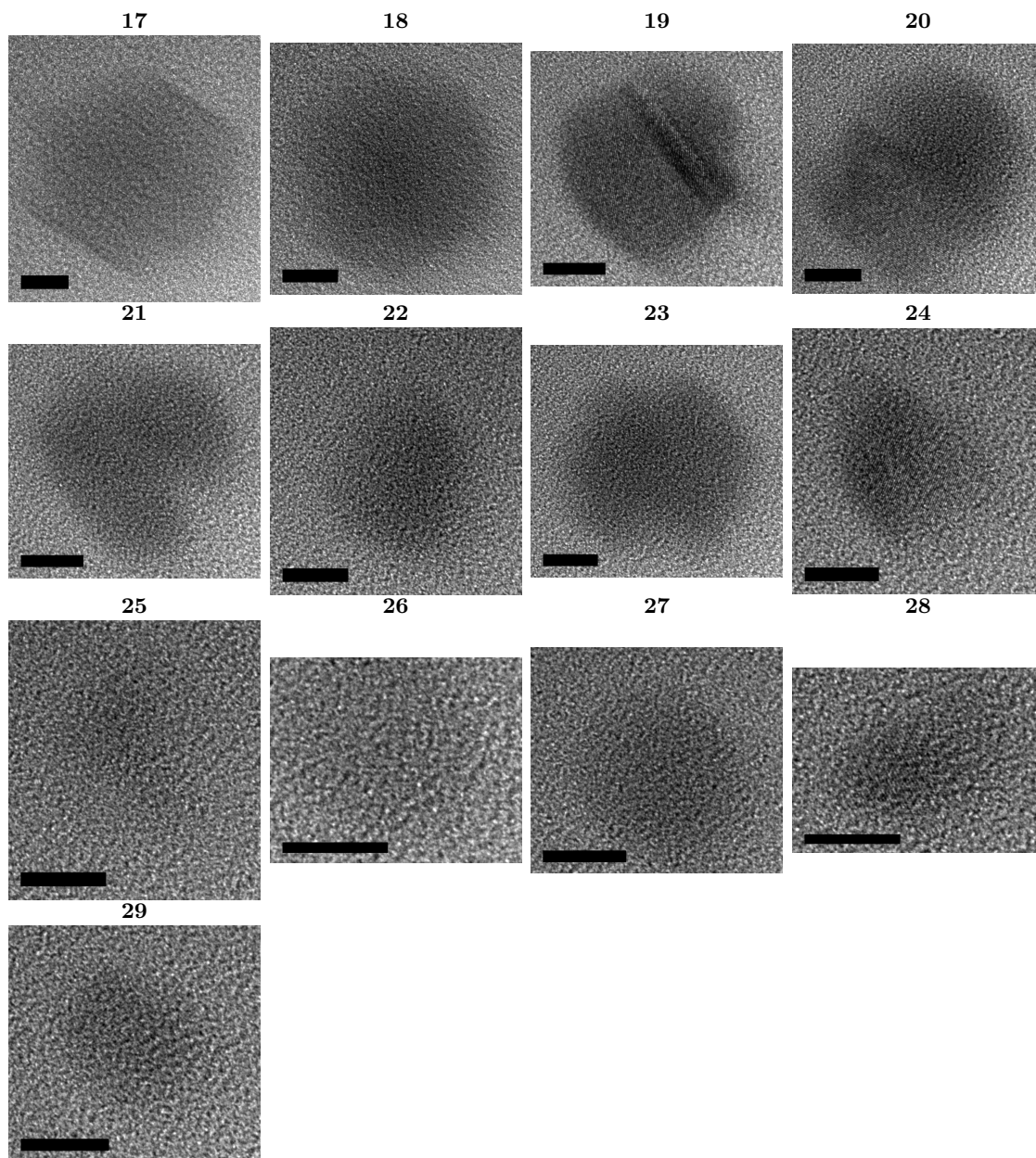


TABLE S3. HRTEM images of the individual magnetosomes 17-29. The scale bar in the images is 5 nm.